


Drag reduction via opposition control in a compressible turbulent channel

Jie Yao * and Fazle Hussain †

Texas Tech University, Department of Mechanical Engineering, Lubbock, Texas 79409, USA

 (Received 24 February 2021; accepted 26 October 2021; published 12 November 2021)

The compressibility effect on opposition drag control is studied via direct numerical simulation of turbulent channel flows at a bulk Reynolds number $Re_b = 3000$ for three different bulk Mach numbers: $M_b = 0.3, 0.8,$ and 1.5 . For all M_b , the drag reduction (DR) has a similar trend as that of the strictly incompressible case; namely, DR first increases and then decreases with the sensing plane location y_d^+ . With increasing M_b , DR slightly decreases at small y_d^+ but increases at large y_d^+ . Consequently, y_d^+ for achieving maximum drag reduction (DR_{\max}) shifts to larger values, namely, from $y_d^+ = 12.5$ for $M_b = 0.3$ to 20 for $M_b = 1.5$, consistent with the outward shift of the peaks of Reynolds stresses at higher M_b . By rescaling the sensing plane with semilocal units, a better collapse of DR is achieved among different M_b , particularly for small y_d^* . The optimal sensing plane is found to be $y_d^* \approx 15$ with $DR_{\max} \approx 23\%$. Interestingly, for large y_d^+ cases, a resonance buffer layer characterized by a streamwise periodic array of spanwise-coherent rollers is established, one of the main reasons for the deterioration of drag reduction performance. This layer of hydroacoustic instability resonance results from the intense interaction of wall-normal wave propagation with the background mean shear. Space-time correlation of wall-normal velocity reveals near-wall organized spanwise structures with a well-defined streamwise wavelength λ_x , decreasing with increasing M_b .

DOI: [10.1103/PhysRevFluids.6.114602](https://doi.org/10.1103/PhysRevFluids.6.114602)

I. INTRODUCTION

Control of wall-bounded turbulent flows to reduce skin-friction drag has significant economical and ecological benefits. Consequently, the recent decades have seen much effort to develop and analyze drag control strategies. One of the promising control techniques is the so-called opposition control (OC), which, based on the sensing on a plane parallel to the wall (called sensing plane), employs local wall blowing/suction to counteract the sweep and ejection motions induced by the near-wall streamwise vortices. Using direct numerical simulation (DNS) of turbulent channel flow, Choi *et al.* [1] achieved approximately 25% drag reduction at the friction Reynolds number $Re_\tau \approx 110$ with the sensing plane located at $y_d^+ = 10$ (The superscript + indicates scaling by wall units, namely, $y^+ = yu_\tau/\nu$). Hammond *et al.* [2] later studied the effect of y_d^+ and found that the maximum drag reduction is obtained when $y_d^+ = 15$, and also showed that, for drag reduced cases, a virtual wall is established halfway between the wall and the sensing plane, through which almost no flow crosses, inhibiting the momentum transfer in the wall-normal direction. Focusing on the effects of both sensing plane y_d^+ and blowing/suction amplitude A , Chung and Talha [3] found that, for a given y_d^+ , drag reduction strongly depends on A . Even for $A < 1$, a substantial drag reduction can still be achieved for $20 < y_d^+ < 30$. In addition, they observed that the maximum drag reduction for different y_d^+ cases is always obtained with the root mean square (r.m.s.) of the wall blowing/suction

*jie.yao@ttu.edu

†fazle.hussain@ttu.edu

velocity $v_w^+ = 0.25$. Xia *et al.* [4] studied the OC in spatially developing turbulent boundary layer and found that 22% drag reduction is obtained after the transient region. Stroh *et al.* [5] compared OC between the turbulent channel and boundary layer flows and showed that in spite of the very similar drag reduction amounts achieved in these two flows, the underlying mechanisms for drag reduction are quite different. While drag reduction is purely based on the attenuation of the Reynolds shear stress in turbulent channel flow, the modification of the spatial flow development is essential for drag reduction in the turbulent boundary layer. The effect of the Reynolds number has also been investigated, where, similar to other methods [6,7], drag reduction slightly decreases with the Reynolds number [8–10]. For example, Wang *et al.* [10] showed that a maximum 20% drag reduction is achieved at $Re_\tau = 1000$ but at a slightly lower sensing plane (i.e., $y_d^+ = 13.5$).

Some other better performing or more practical control methods have also been proposed and investigated based on this simple technique. For example, Lee *et al.* [11] developed the suboptimal control, using information measurable at the wall only, e.g., streamwise wall-shear stress, spanwise wall-shear stress, and wall pressure. Koumoutsakos [12] also proposed a control based on vorticity flux, where 40% drag reduction was achieved at $Re_\tau = 180$. Pamiès *et al.* [13] employed the blowing-only OC to improve drag control performance. Inspired by Choi *et al.* [1]’s work, Wang *et al.* [10] investigated OC using both wall-normal and spanwise velocity components, where more drag reduction and control efficiency can be achieved when spanwise velocity is included. Recently, Yao *et al.* [14] developed a composite control strategy by integrating OC with the spanwise opposite wall-jet method [7,15], yielding a much higher drag reduction than each individual method. Lee *et al.* [16] applied a neural network in a turbulent channel flow at $Re_\tau = 100$ and obtained 18% drag reduction using spanwise wall-shear stress to predict wall-normal velocity at $y_d^+ = 10$. Machine learning is now becoming one of today’s most rapidly growing techniques. Han and Huang [17] pursued the feasibility of employing a convolutional neural network (CNN) to predict the wall-normal velocity on the sensing plane using either spanwise or streamwise wall-shear stress generated from DNS. Applying the trained CNNs to a low Reynolds number (i.e., $Re_\tau = 100$), they obtained 19% and 10% drag reduction based on spanwise and streamwise wall-shear stresses, respectively. Similarly, Park and Choi [18] also found that up to 18% drag reduction can be achieved using CNNs at $Re_\tau = 180$. In addition, 15% drag reduction can still be obtained at $Re_\tau = 578$ by applying the CNN trained at $Re_\tau = 180$. Due to the large computational cost of DNS at high Re , some low-order flow models have been developed for drag control studies [19,20]. For example, Luhar *et al.* [20] analyzed OC using a low-order model based on the resolvent analysis and showed that the model could qualitatively capture the changes in drag reduction with sensing plane and Reynolds number observed in DNS. In addition, they also extend OC from the physical domain to a Fourier domain perspective (the so-called varying-phase opposition control), which allows the controller amplitude for each mode to be complex [21].

Due to its practical relevance, drag control in compressible flow has also been extensively studied, particularly for passive and open-loop active methods. Duan and Choudhari [22,23] found a 7% drag reduction by DNS of hypersonic turbulent boundary layers over riblets. Zhe *et al.* [24] investigated the effects of uniform blowing or suction on the skin friction in hypersonic turbulent boundary layers at a free-stream Mach number of 6. They demonstrated that uniform blowing reduces the skin friction while uniform suction increases it, similar as in the incompressible cases [25,26]. Kametani *et al.* [27] studied uniform blowing/suction in compressible turbulent channel flow (CTCF) and found that the drag reduction and the net energy savings are hardly affected by the Mach number. Fang *et al.* [28] carried out a large eddy simulation of CTCF under spanwise wall oscillation at a bulk Mach number of 0.5, with emphasis on heat transport and its relationship with momentum transport. Recently, we studied the effectiveness of spanwise wall oscillation in CTCF [29] and found that at the same semilocal Reynolds number, drag reduction as a function of oscillation period exhibits good agreement between the supersonic and incompressible cases when using semilocal scaling.

Our main objective here is to study the compressibility effect of OC in CTCF. The rest of the paper is organized as follows. In Sec. II, the governing equation, numerical scheme, and control method are described. Then, the drag reduction results are presented in Sec. III. To elucidate the underlying mechanism of skin-friction variation under control, flow statistics, and coherent structures are examined in Sec. IV. Section V compares the strictly incompressible and low Mach number cases and discusses the properties of the resonance buffer layer observed for large y_d cases. Finally, conclusions are drawn in Sec. VI.

II. COMPUTATIONAL APPROACH

A. Governing equations

We consider flows of a perfect gas, governed by the compressible Navier-Stokes equations

$$\frac{\partial \rho}{\partial t} + \frac{\partial \rho u_i}{\partial x_i} = 0, \quad (1)$$

$$\frac{\partial \rho u_i}{\partial t} + \frac{\partial \rho u_i u_j}{\partial x_j} = -\frac{\partial p}{\partial x_i} + \frac{\partial \sigma_{ij}}{\partial x_j} + f_i, \quad (2)$$

$$\frac{\partial e}{\partial t} + \frac{\partial (e + p)u_j}{\partial x_j} = \frac{\partial \sigma_{ij}u_i - q_j}{\partial x_j} + f_i u_i, \quad (3)$$

where ρ is the density, u_i the velocity component in the i th direction, p the pressure, q_j and σ_{ij} are the components of the heat flux vector and the viscous stress tensor, and e is the total energy per unit volume, which is the sum of internal energy e_s and kinetic energy $e = \rho(e_s + u_i u_i/2)$. The Einstein summation convention applies to the repeated indices.

For the perfect gas, the thermal and caloric equation of state (EOS) is $p = \rho RT$, with R the universal gas constant. The internal energy is a function of the temperature only $e_s = c_v T$, with c_v the specific heat at constant volume, and $c_p = R/(\gamma - 1)$, $\gamma = c_p/c_v$ is the specific heat ratio, and c_p the specific heat at constant pressure.

The viscous stress and the heat flux are defined as

$$\sigma_{ij} = 2\mu \left(S_{ij} - \frac{1}{3} \delta_{ij} S_{kk} \right), \quad (4)$$

$$q_j = -k \frac{\partial T}{\partial x_j}, \quad (5)$$

where μ is the dynamical viscosity, $S_{ij} = (u_{i,j} + u_{j,i})/2$ is the rate of the strain tensor, and $k = c_p \mu / Pr$ is the thermal conductivity. The viscosity is assumed to obey Sutherland's law

$$\mu = \mu_0 \frac{T_0 + S}{T + S} \left(\frac{T}{T_0} \right)^{3/2}, \quad (6)$$

where μ_0 and T_0 are reference values and S is a constant. Throughout, $S = 110.4$ K and $T_0 = 293.15$ K, and the Prandtl number $Pr = 0.72$ [30].

B. Numerical scheme and simulation parameters

DNSs of the compressible turbulent channel flows are performed with an in-house code. The streamwise, the wall-normal, and the spanwise coordinates are represented by x , y , z , respectively; the corresponding velocity components are u , v , w . The governing equations are discretized using the finite difference method with a seventh-order upwind-biased scheme for the convective terms and an eighth-order centered scheme for the viscous terms. The time integration is done by using the low-storage third-order Runge-Kutta scheme. The flow is assumed to be periodic in the x and z directions, where the uniform mesh is used, and a mapping function is used in the y direction to cluster mesh points towards the wall.

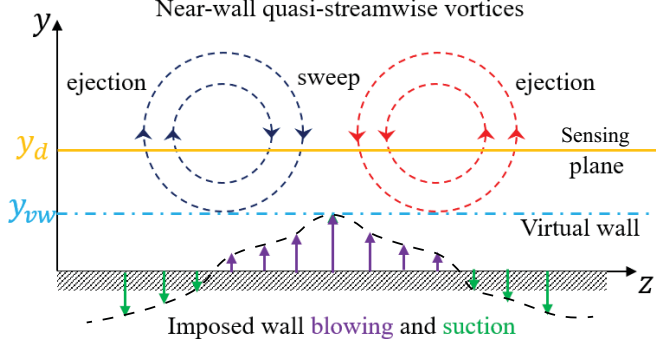


FIG. 1. Schematic of the opposition drag control.

In order to enforce a constant mass-flow rate in time, a spatially constant body force f_1 is applied in the streamwise direction [31], and the corresponding power spent is added to the right-hand side of the total energy equation. The isothermal wall boundary condition is employed for the temperature. For the uncontrolled case, the no-slip boundary conditions are applied on both walls, i.e., $(u_i)_w = 0$. For the case with OC (Fig. 1), the wall-normal velocity at the wall is set as

$$v_w(x, z, t) = -A[\rho v](x, y_d, z, t)/\rho_w(x, z, t), \quad (7)$$

where A is the control amplitude, $[\rho v](y_d)$ is the wall-normal mass flux at the sensing plane y_d , and ρ_w is the density at the wall (hereinafter, subscript w represents the quantity value on the wall). Note that instead of solely using wall-normal velocity v as in incompressible cases [1,3], the wall-normal mass flux ρv is employed here. This is because due to the high density near the wall, the control based only on wall-normal velocity v is found to be very unstable for large y_d^+ cases. The requirement of simultaneously measuring velocity and density in the flow certainly poses great challenges in practical applications; however, this issue is beyond the scope of the current paper.

The bulk Reynolds and Mach number are defined as $Re_b = \rho_b U_b / \mu_w$ and $M_b = U_b / c_w$, where μ_w and c_w are the dynamical viscosity on the wall and speed of sound at the wall temperature; and bulk density ρ_b and bulk mean velocity U_b are defined as

$$\rho_b = \frac{1}{2\delta} \int_0^{2h} \bar{\rho} dy, \quad U_b = \frac{1}{2\delta \rho_b} \int_0^{2h} \bar{\rho} u dy, \quad (8)$$

with h denoting the half-channel height. Hereinafter, overbar $(\bar{\cdot})$ denotes Reynolds averaging in the homogeneous space direction and in time.

Simulations are performed at a fixed bulk Reynolds number $Re_b = 3000$ with three different bulk Mach numbers $M_b = 0.3, 0.8,$ and 1.5 . The computational domain has dimensions $L_x \times L_y \times L_z = 6\pi h \times 2h \times 2\pi h$ in streamwise (x), wall-normal (y), and spanwise (z) directions, respectively. The simulation parameters are listed in Table I. The domain sizes and grid resolutions are the same as those used in Ref. [32]. The friction Reynolds number is defined as the ratio of outer to

TABLE I. Details of the numerical discretization employed in the simulations. The computational box size is $6\pi h \times 2h \times 2\pi h$ for all cases, and $N_x, N_y,$ and N_z are the grid sizes in each direction.

| Case | Re_b | Re_τ | Re_τ^* | M_b | $N_x \times N_y \times N_z$ | Δx^+ | Δy^+ | Δz^+ |
|--------|--------|-----------|-------------|-------|-----------------------------|--------------|--------------|--------------|
| C3KM03 | 3000 | 191 | 197 | 0.3 | $384 \times 129 \times 192$ | 9.4 | 0.45 – 6.2 | 6.2 |
| C3KM08 | 3000 | 198 | 174 | 0.8 | $384 \times 129 \times 192$ | 9.7 | 0.47 – 6.4 | 6.5 |
| C3KM15 | 3000 | 219 | 144 | 1.5 | $512 \times 129 \times 256$ | 8.1 | 0.52 – 7.1 | 5.4 |

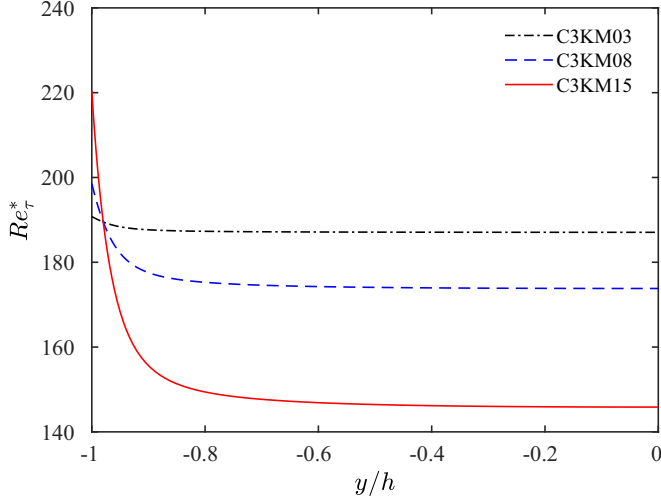


FIG. 2. Semilocal Reynolds number Re_τ^* as a function of y/h for $Re_b = 3000$ at different M_b cases.

viscous length scales ($\delta_v = \nu_w/u_\tau$, where $u_\tau = \sqrt{\tau_w/\rho_w}$ is the friction velocity and $\nu = \mu/\rho$ is the kinematic viscosity); hence, $Re_\tau = h/\delta_v = u_\tau h/\nu_w$. Recent studies [33,34] show that better collapse of the flow statistics with incompressible flows can be obtained by normalizing the mean velocity and Reynolds stress with respect to suitable semilocal wall units [35] based on the local density and viscosity (i.e., $u_\tau^* = \sqrt{\tau_w/\bar{\rho}}$, $\delta_v^* = \bar{\nu}/u_\tau^*$). Accordingly, the semilocal Reynolds number is defined as $Re_\tau^* = h/\delta_v^* = Re_\tau \sqrt{(\bar{\rho}/\rho_w)}/(\bar{\mu}/\mu_w)$. Hereinafter, quantities made nondimensional with respect to semilocal wall units are denoted with superscript *. Figure 2 shows the distribution of Re_τ^* as a function of y/h for different M_b cases. For an isothermal CTCF, $Re_\tau^* = Re_\tau$ at the wall and decreases towards the channel center. In addition, the rate of decrease increases with M_b , especially at the near-wall region.

In the current study, the control amplitude is fixed at $A = 1$, and the sensing-plane locations are varied between $5 \leq y_d^+ \leq 30$. For each M_b , only the cases that can yield drag reduction are considered. Note that no interpolation was applied to obtain the velocity at a sensing plane. Instead, the sensing plane was chosen as the nearest grid point. For example, the sensing plane for $y_d^+ = 15$ at $M_b = 0.8$ is not located exactly at $y^+ = 15$ but at the nearest grid point, which is at $y^+ = 14.6$. The exact locations are summarized in Table II, and the nominal values in the table are later referred to as the sensing-plane locations. All computations start with the same initial condition of an uncontrolled fully developed flow at the same Re_b and M_b .

TABLE II. Details of the sensing-plane locations. y_d^+ and $y_d^* = y_d^+ \sqrt{(\bar{\rho}/\rho_w)}/(\bar{\mu}/\mu_w)$ are the sensing-plane location in wall and semilocal units, respectively.

| Case | 1 | 2 | 3 | 4 | 5 | 6 | 7 | 8 | 9 | 10 | |
|--------|----------------|-----|-----|-----|------|------|------|------|------|------|------|
| | nominal values | 5 | 7.5 | 10 | 12.5 | 15 | 17.5 | 20 | 22.5 | 25 | 30 |
| C3KM03 | y_d^+ | 5.2 | 7.7 | 9.5 | 12.8 | 15.3 | 18.0 | — | — | — | — |
| | y_d^* | 5.2 | 7.6 | 9.4 | 12.6 | 15.0 | 17.8 | — | — | — | — |
| C3KM08 | y_d^+ | 4.7 | 7.1 | 9.9 | 12.1 | 14.6 | 17.3 | 20.4 | 22.1 | 25.7 | — |
| | y_d^* | 4.4 | 6.6 | 9.1 | 11.0 | 13.2 | 15.6 | 18.2 | 19.7 | 22.8 | — |
| C3KM15 | y_d^+ | 5.2 | 7.8 | 9.9 | 12.1 | 14.7 | 17.6 | 20.8 | 22.5 | 24.3 | 30.5 |
| | y_d^* | 4.3 | 6.2 | 7.6 | 9.1 | 10.8 | 12.7 | 14.7 | 15.8 | 17.0 | 21.0 |

TABLE III. Details of the numerical discretization employed for the incompressible turbulent channel simulations. The computational box size is $4\pi h \times 2h \times 2\pi h$ for all cases, and N_x , N_y , and N_z are the numbers of grid sizes.

| Case | Re_b | Re_τ | $N_x \times N_y \times N_z$ | Δx^+ | Δy^+ | Δz^+ |
|--------|--------|-----------|-----------------------------|--------------|--------------|--------------|
| I3KM00 | 3180 | 200 | $256 \times 128 \times 256$ | 6.9 | 0.08 – 3.3 | 4.6 |

For comparison, drag control for strictly incompressible flows at friction Reynolds number $Re_\tau = 200$ is also carried out. The numerical details are provided in Table III. The code used for the incompressible case is the same as the one used in our previous studies [14,36], built around the main solver developed by Ref. [37]. Using the method in Ref. [38], the incompressible Navier-Stokes equations are solved based on the equations for the wall-normal vorticity and the Laplacian of the wall-normal velocity. This formulation has the advantage of satisfying the continuity constraint exactly while eliminating the pressure. A Fourier-Galerkin method is used in the streamwise and spanwise directions, while a seventh-order B-spline collocation method is employed in the wall-normal direction. A low-storage implicit-explicit scheme based on third-order Runge-Kutta for the nonlinear terms and Crank-Nicolson for the viscous terms are used for time advance. The flow is driven by a pressure gradient, which is adjusted in time to ensure that the mass flux through the channel always remains constant. For more details about the numerical methods, see Ref. [37].

III. DRAG REDUCTION

Since the mass-flow rate is kept constant during the simulation, drag reduction can be quantified as a relative change in the skin-friction coefficient:

$$DR = 1 - C_f/C_{f,0}, \tag{9}$$

where $C_f = 2\tau_w/(\rho_b U_b^2)$ and $C_{f,0} = 2\tau_{w,0}/(\rho_b U_b^2)$ are the drag coefficients of the controlled and reference (uncontrolled) cases, respectively.

Figure 3(a) shows the drag reduction DR as a function of the sensing-plane location y_d^+ for all M_b cases along with that for the (strictly) incompressible case. The effectiveness of OC is very sensitive to y_d^+ . For the incompressible case, DR gradually increases with y_d^+ to a maximum and then decreases. Consistent with previous results [2,3], the optimal sensing-plane location $y_{d,opt}^+$ is around 15, and the associated maximum drag reduction $DR_{max} \approx 22.8\%$. Overall, DR for the compressible

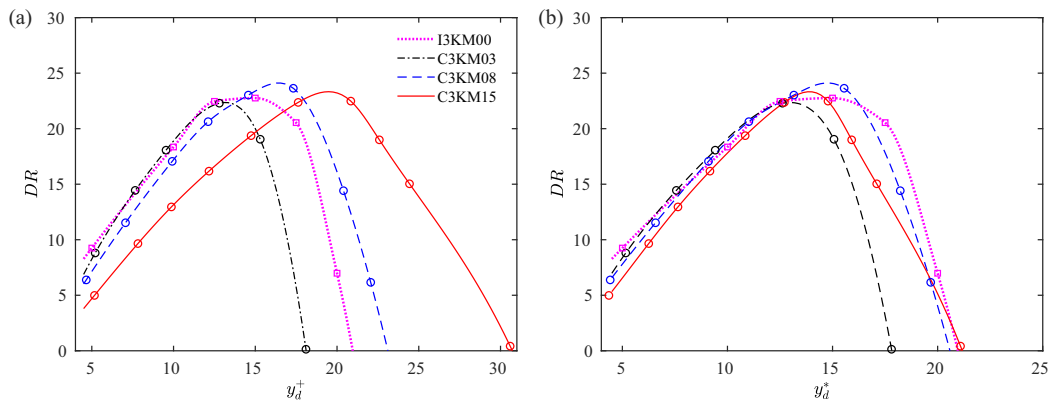


FIG. 3. Drag reduction (DR) as a function of (a) y_d^+ and (b) y_d^* .

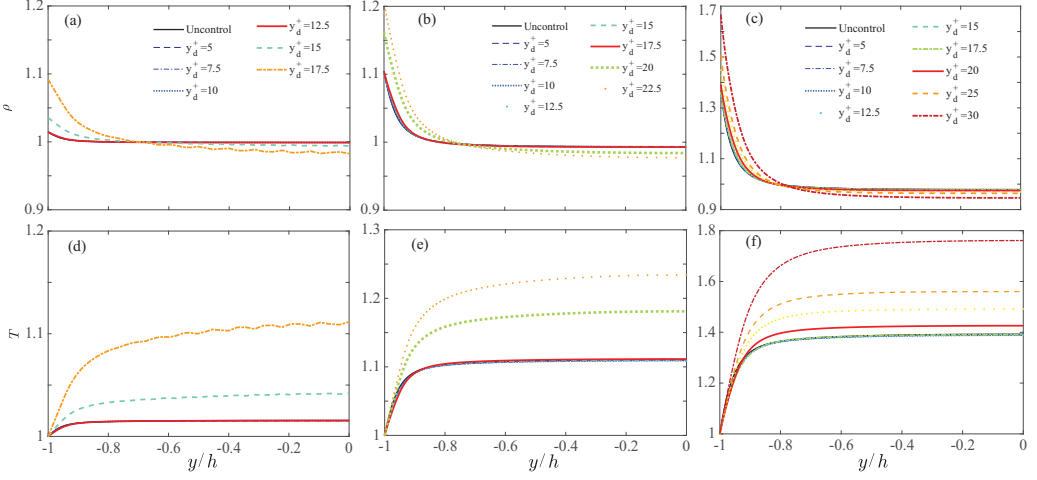


FIG. 4. Mean density $\bar{\rho}$ (a)–(c) and temperature \bar{T} (d)–(f) profiles for different y_d^+ cases at (a), (d) $M_b = 0.3$, (b), (e) $M_b = 0.8$, and (c), (f) 1.5 with $Re_b = 3000$.

cases exhibits similar trends as the incompressible one. At small y_d^+ , DR for $M_b = 0.3$ agrees well with the incompressible case and slightly decreases with increasing M_b ; at large y_d^+ , DR for $M_b = 0.3$ case deviates from the incompressible case. The optimal DR occurs at lower y_d^+ for $M_b = 0.3$ case. Such deviation is very interesting and will be discussed in detail later. In addition, at large y_d^+ , the rate of decrease of DR with respect to y_d^+ becomes smaller as M_b increases, resulting in a larger DR at higher M_b . Consequently, the y_d^+ range for achieving positive DR is much broader at higher Re. In particular, the range for $DR > 0$ increases from $0 < y_d^+ < 17.5$ to $0 < y_d^+ < 30$ when M_b changes from 0.3 to 1.5. This enlarge of y_d^+ range can extend the applicability of OC for the supersonic and hypersonic cases, especially at high Re, since strictly sticking to a particular y_d^+ is not required. Although the maximum drag reduction DR_{\max} does not vary significantly with M_b , the sensing-plane location $y_{d,\text{opt}}^+$ for achieving DR_{\max} increases with increasing M_b . In particular, $y_{d,\text{opt}}^+$ becomes 12.5, 17.5, and 20 for $M_b = 0.3, 0.8$, and 1.5, respectively; and the corresponding $DR_{\max} = 22.3\%, 23.6\%$, and 22.1% , very close to the DR_{\max} obtained for the incompressible cases. The change in $y_{d,\text{opt}}^+$ with M_b is consistent with the outward shift of the peak turbulence intensity (discussed in Sec. IV C).

Note that previous results [34,35,39] showed that good collapses between incompressible and compressible cases could be obtained for the mean velocity and Reynolds stresses in semilocal coordinates y^* is employed. In addition, in the study of spanwise wall oscillation drag control in CTCF [29], we found that when scaling the control parameters using the semilocal unit, a better agreement can be obtained between incompressible and compressible cases. Hence, it is interesting to examine DR as a function of sensing-plane location in semilocal units y_d^* . Figure 3(b) clearly shows that DR agrees better among different M_b cases, particularly at small y_d^* . The location of the sensing plane for achieving DR_{\max} is roughly at $y_{d,\text{opt}}^* \approx 15$ for all M_b cases. The larger discrepancy of DR_{\max} at large y_d^* between different cases is due to the resonance in the buffer layer to be discussed later.

IV. FLOW PHYSICS

A. Mean density and temperature profiles

Profiles of the Reynolds-averaged density $\bar{\rho}$ and temperature \bar{T} for different y_d^+ are displayed in Fig. 4. For all M_b cases, \bar{T} rises steeply near the wall and reaches a plateau in the core region;

correspondingly, $\bar{\rho}$ decreases rapidly near the wall and then reaches a plateau in the channel core [40]. The temperature at the center of the channel \bar{T}_c and density at the wall $\bar{\rho}_w$ increase with M_b , which is due to enhanced viscous heating. Under OC, while \bar{T} is almost unchanged for small y_d^+ cases, it increases significantly for larger y_d^+ case, which is attributed to the formation of organized near-wall spanwise structures due to flow resonance [e.g., Figs. 11(f), 11(h) 11(i)]. Accordingly, $\bar{\rho}$ at the wall also increases, but it is only slightly altered in the core region, where the compressible effect is rather weak. The variation of these thermodynamic properties, particularly for the large y_d^+ cases, will be shown to play a role in affecting the drag control performance. This is different from the results reported by Kametani *et al.* [27] for drag control using uniform blowing and suction, where $\bar{\rho}_w$ and \bar{T}_c are not significantly altered.

B. Mean streamwise velocity profiles

When the compressibility effect is present, instead of using classical wall unit scaling, the van Driest transformation [41] ($U_d^+ = \int_0^{U^+} \sqrt{\bar{\rho}/\bar{\rho}_w} dU^+$), which can incorporate the density variation effect, is often employed to collapse the velocity profiles of supersonic flows with those of incompressible flows. Although this transformation has been shown to work for supersonic flows over adiabatic walls [42–44], it fails to capture the correct intercept of the log law for diabatic walls, especially when strong heat flux is present [42]. To overcome this drawback, Trettel and Larsson [33] derived a new transformation

$$U^* = \int_0^{U^+} \sqrt{\frac{\bar{\rho}}{\bar{\rho}_w}} \left[1 + \frac{1}{2\bar{\rho}} \frac{d\bar{\rho}}{dy} y - \frac{1}{\bar{\mu}} \frac{d\bar{\mu}}{dy} y \right] dU^+, \quad (10)$$

which has been shown to collapse very well the mean velocity profiles for supersonic channel flows with isothermally cooled walls [32,34].

The mean velocity profiles based on both the van Driest and Trettel-Larsson transformations under OC for different y_d^+ are displayed in Fig. 5. Under control, similar to the incompressible cases [3,45], the velocity profiles in the outer region show a characteristic upward or downward shift. Consistent with that observed in Ref. [29], the magnitude of the shift is roughly proportional to DR, particularly under the Trettel-Larsson transformation. Different from other control methods, such as riblets [46] and spanwise wall oscillation [29,47], the mean velocity profiles under OC control deviate from the law of the wall. In particular, it undershoots the uncontrolled one in the viscous sublayer, which is due to a smaller velocity gradient caused by the nonzero limiting behavior of the Reynolds shear-stress gradient in the near wall (inset in Fig. 7).

C. Reynolds stresses

The effect of control on Reynolds stresses ($\tau_{ij} = \bar{\rho} R_{ij}$, with $R_{ij} = \widetilde{u_i' u_j'}$ = $\widetilde{u_i u_j} - \widetilde{u_i} \widetilde{u_j}$) is further scrutinized. (Hereinafter, $\widetilde{\phi}$ represents Favre averaging defined as $\widetilde{\phi} = \overline{\phi \bar{\rho}} / \bar{\rho}$, with ϕ'' denoting the remaining fluctuations.) Figures 6 and 7 show the Reynolds normal (τ_{11} , τ_{22} , and τ_{33}) and shear (τ_{12}) stresses as a function of y_0^+ for different y_d^+ cases, respectively. Note that to highlight the absolute changes under control, the Reynolds stresses are normalized with the uncontrolled wall-shear stress $\tau_{w,0}$. (Hereinafter, the subscript 0 denotes the value of uncontrolled case.) For the uncontrolled case, the peak value of τ_{11} increases as M_b increases, but the peak of wall-normal Reynolds stress τ_{22} , spanwise Reynolds stress τ_{33} , and Reynolds shear stress τ_{12} decrease with increasing M_b . As explained in Refs. [32,48], the increase of the τ_{11} peak at high M_b is due to increased mean shear (dU/dy). In addition, as M_b increases, flow temperature, as well as viscosity, increases, suppressing the ejection and sweep events of near-wall streamwise vortices, thus leading to lower values of the peak in τ_{22} and τ_{33} . The peak locations of all the Reynolds stresses in wall units increases with M_b ,

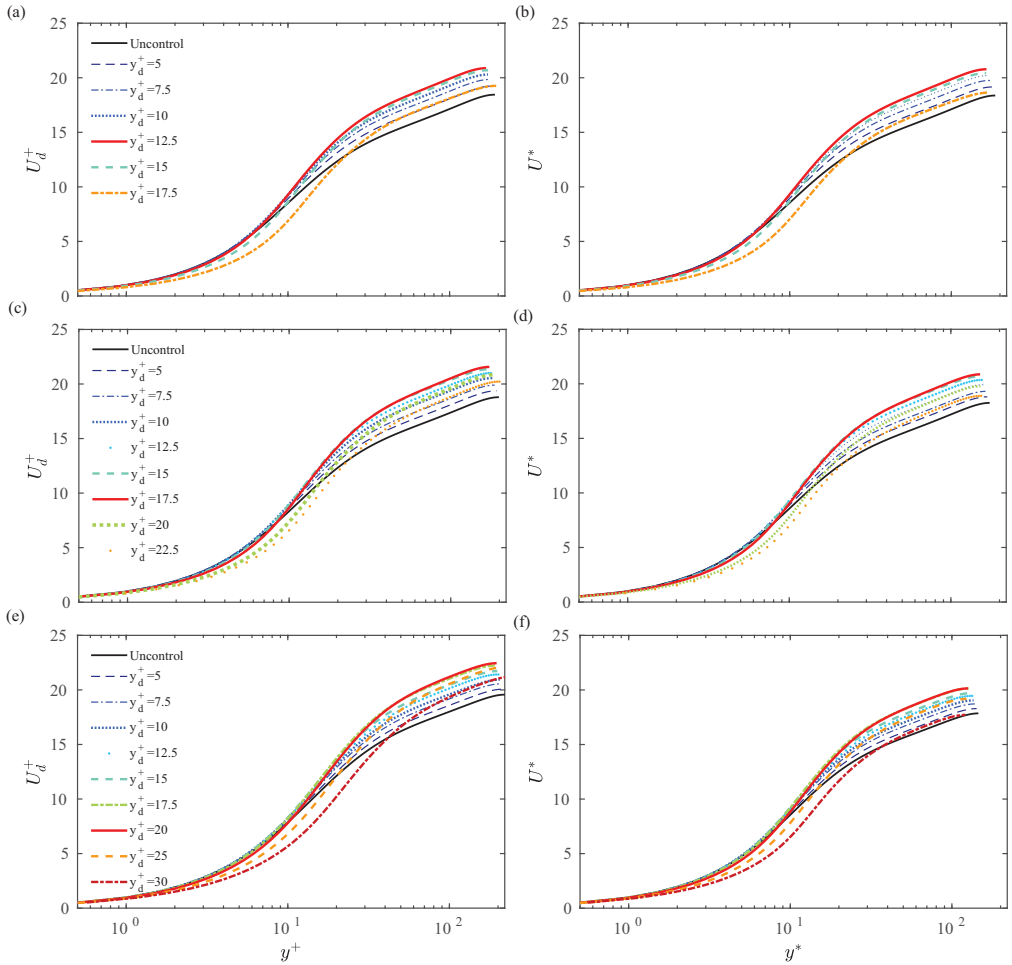


FIG. 5. Transformed mean streamwise velocity profiles for different sensing plane y_d^+ cases at (a), (b) $M_b = 0.3$; (c), (d) $M_b = 0.8$; (e), (f) $M_b = 1.5$. The left and right rows represent the van Driest transformation and the Trettel-Larsson transformation, respectively.

which is consistent with the finding that $y_{d,\text{opt}}^+$ becomes larger at higher M_b . References [32,34,39] showed that the Reynolds stresses collapse with the incompressible cases when scaled with the semilocal unit, with the only exception that the τ_{11} peak increases with Mach number. This also explains why DR between different M_b cases collapse better when using y_d^*

As shown in Refs. [1,3], OC establishes a virtual wall, which is typically located halfway between the physical wall and the sensing plane y_d^+ . Hence, as y_d^+ increases, the virtual wall gradually moves away from the wall. For the incompressible case [45], the virtual wall location y_{vw} can be identified by a local minimum of the wall-normal Reynolds stress τ_{22} or Reynolds shear stress τ_{12} . However, it is clear from Figs. 6(d)–6(f) that the correspondence between the location of virtual wall $y_{vw} = y_d^+/2$ and the local minimum of τ_{22} disappears, especially for the large y_d^+ cases at $M_b = 1.5$. Figure 8 further shows the local minimum location of τ_{22} and τ_{12} as functions of y_d^+ for all M_b cases. For small y_d^+ cases, the local minimum location of τ_{22} agrees with the virtual wall location $y_{vw} = y_d^+/2$, but starts to deviate at large y_d^+ . For $M_b = 1.5$ case, the location of the local minimum moves even towards the wall when $y_d^+ \geq 20$. On the other hand, the location of the local minimum of τ_{12} is

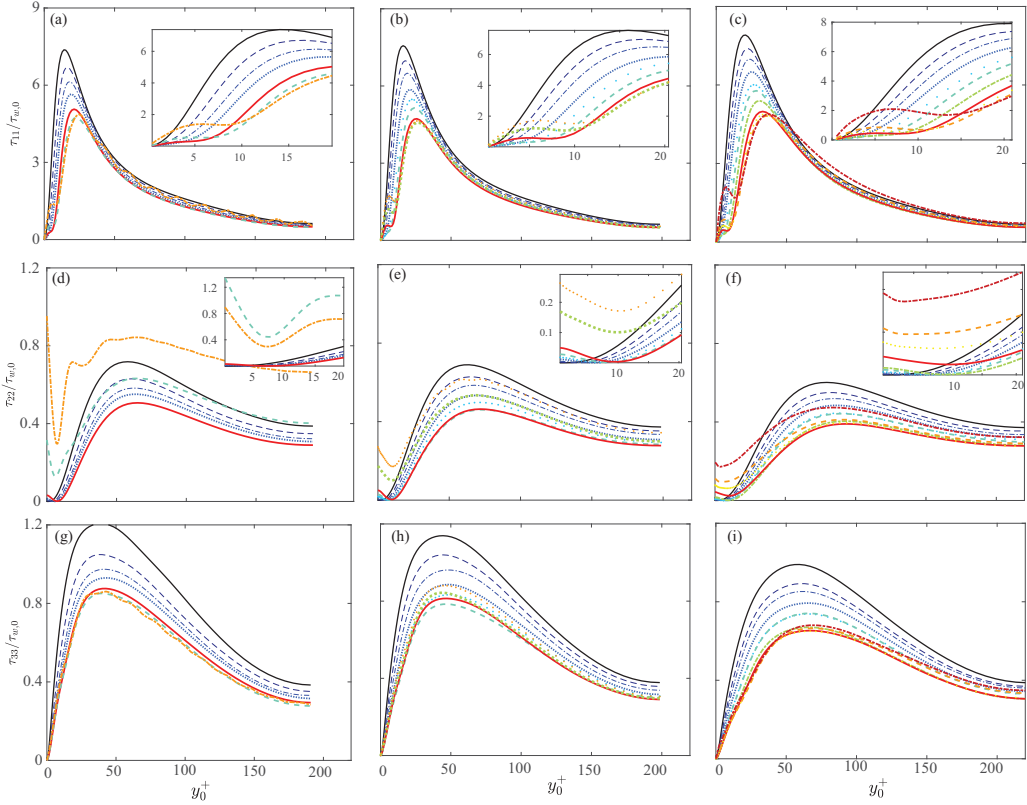


FIG. 6. Reynolds normal stresses components (normalized by the wall-shear stress of the uncontrolled case $\tau_{w,0}$) as a function of y_0^+ for different y_d^+ cases: (a)–(c) τ_{11} ; (d)–(f) τ_{22} ; (g)–(i) τ_{33} . The left, middle, and right columns correspond to $M_b = 0.3, 0.8$ and 1.5 cases, respectively. See Fig. 5 for the legends of the curves.

found to well match the virtual wall y_{vw} [Fig. 8(b)]. This is because the OC considered here is designed based on wall-normal mass flux ρv ; hence the density distribution plays a significant role in positioning the minimum of τ_{22} as well as the virtual wall. As density ρ is maximum at the wall and rapidly decreases along the wall-normal direction, especially for large y_d^+ case, the local minimum of $\tau_{22} = \overline{\rho v^2} = (\rho v)^2/\rho$ is more biased towards the wall. Although the virtual wall effect

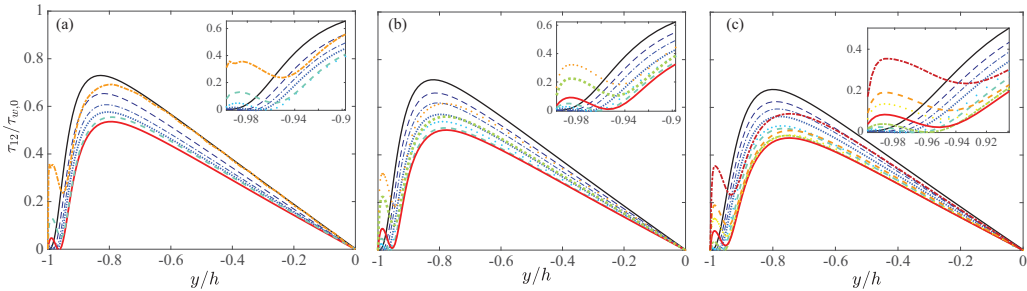


FIG. 7. Reynolds shear stress τ_{12} (normalized by the wall-shear stress of the uncontrolled case $\tau_{w,0}$) as a function of y_0^+ for different y_d^+ : (a) $M_b = 0.3$, (b) $M_b = 0.8$, and (c) $M_b = 1.5$. See Fig. 5 for the legends of the curves.

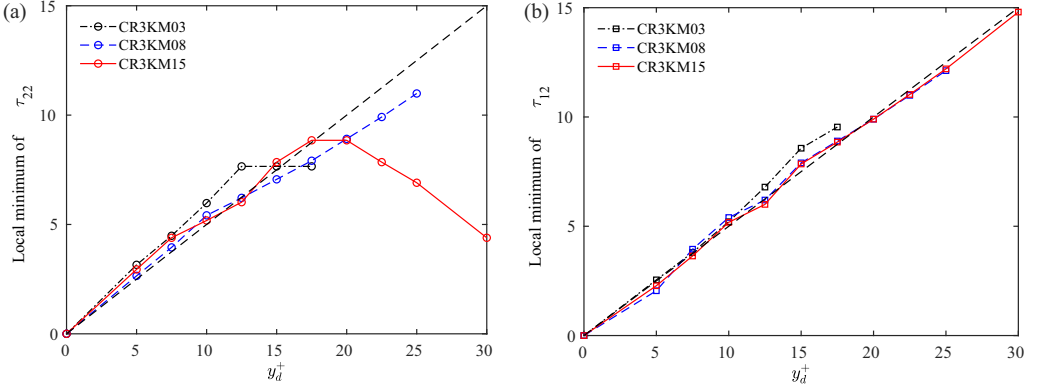


FIG. 8. The location of near-wall local minimum of (a) τ_{22} and (b) τ_{12} . The back dashed line denotes $y = y_d^+/2$

is not apparent on spanwise Reynolds stress τ_{33} , it also occurs in the distribution of τ_{11} . A plateau is formed around the virtual wall, and gradually evolves to a local minimum as y_d^+ increases.

Near the virtual wall, turbulent intensities are significantly suppressed. In particular, τ_{22} and τ_{11} become almost zero at the virtual wall for the optimally controlled case, which inhibits the interaction between the near wall and the core regions. Due to the actuation applied at the wall, namely, opposite blowing/suction, the wall-normal Reynolds stress τ_{22} and shear stress τ_{12} are enhanced very close to the wall. When the sensing plane is farther away from the wall, τ_{12} below the virtual wall significantly increases, which is the key factor of deterioration of drag control performance [2]. In addition, all the Reynolds stresses are suppressed above the virtual wall for the drag reduction cases, especially for the optimal control cases. Compared to the uncontrolled case, the peak location moves away from the wall under control, which is consistent with the observation in the strictly incompressible cases [1,45] as well as for other control methods [15,49].

D. Skin-friction decomposition

Based on the FIK identity [50,51], the total skin friction can be expressed as

$$C_f = \underbrace{\frac{6}{\text{Re}_b}}_{C_f^L} + 3 \underbrace{\int_{-1}^1 y \bar{\rho} \widetilde{u''v''} dy}_{C_f^T} + \underbrace{\frac{3}{\text{Re}_b} \int_{-1}^1 y \left(\frac{\bar{\mu}}{\bar{\mu}_w} - 1 \right) \frac{\partial \bar{u}}{\partial y} dy}_{C_f^\mu} + \underbrace{\frac{3}{\text{Re}_b} \int_{-1}^1 y \mu' \left(\frac{\partial u'}{\partial y} + \frac{\partial v'}{\partial x} \right) dy}_{C_f^{\mu T}},$$

which decomposes the skin friction into four components: (i) an equivalent laminar part C_f^L , (ii) a turbulent part C_f^T represented by the weighted integration of the total Reynolds shear stress, (iii) the compressible contribution C_f^μ related to the mean viscosity variations and the mean wall-normal velocity gradient, and (iv) the compressible-turbulent interaction part $C_f^{\mu T}$.

Figures 9(a)–9(c) show the skin-friction decomposition as a function of y_d^+ for $M_b = 0.3$, 0.8, and 1.5 cases, respectively. For the uncontrolled case, C_f^L contributes approximately 25% of the total C_f , the compressible-turbulent interaction term $C_f^{\mu T}$ is negligible, and the compressible contribution term C_f^μ is also small—approximately 0.3% at $M_b = 0.3$, 1.3% at $M_b = 0.8$, and 4.5% at $M_b = 1.5$. Hence, the turbulent part C_f^T is the dominant contribution for the total C_f (similar to the incompressible case), and its contribution gradually decreases as M_b increases, being 75.0%, 73.5%, and 69.8% at $M_b = 0.3$, 0.8, and 1.5, respectively.

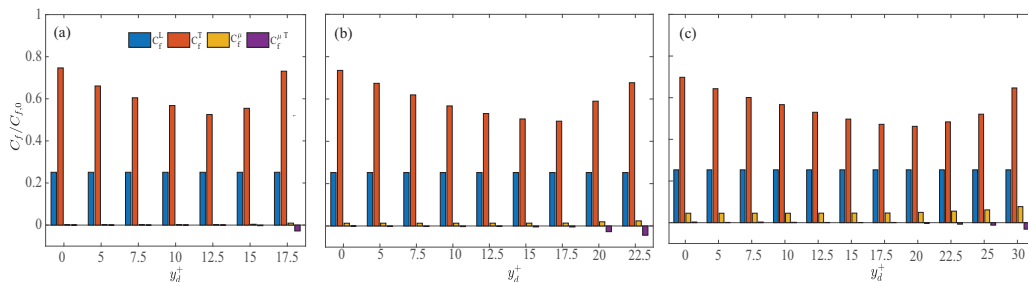


FIG. 9. Decomposed skin friction C_f for different y_d^+ at: (a) $M_b = 0.3$, (b) $M_b = 0.8$; and (c) 1.5. Note that $y_d^+ = 0$ denotes the uncontrolled case.

Under control, since Re_b is fixed, C_f^L is held constant for all cases. C_f^μ is negligible at $M_b = 0.3$ and slightly increases with y_d^+ at $M_b = 0.8$. For example, $C_f^\mu / C_{f,0}$ increases to approximately 2.4% for $y_d^+ = 22.5$ at $M_b = 0.8$. For the $M_b = 1.5$ case, the contribution of C_f^μ further increases, in particular, increasing to approximately 7.7% of the total $C_{f,0}$ at $y_d^+ = 30$. Figure 9 shows that, even for $M_b = 1.5$ case, the reduction (or increase) in total C_f is mainly due to the decrease (or increase) in C_f^T (corresponding to the suppression of the turbulent Reynolds shear stress). Although C_f^T at $M_b = 1.5$ is comparable to that of $M_b = 0.8$ cases for small y_d^+ , it is much smaller than that of $M_b = 0.8$ for large y_d^+ , which is consistent with a larger DR (Fig. 3). It is interesting to observe that, for large y_d^+ cases, when drag reduction deteriorates, C_f^T rapidly increases, which is counterbalanced by the negative contribution from $C_f^{\mu T}$. For example, for $y_d^+ = 22.5$ at $M_b = 0.8$, C_f^T contributes about 67% of the total $C_{f,0}$, but C_f^μ becomes approximately -4.4% . The negative C_f^μ can be qualitatively explained as follows. At the sweep (high-speed streak) regions (Fig. 1), the streamwise velocity fluctuations $u' > 0$, hence $\partial u' / \partial y > 0$ (since $u' = 0$ at the wall). Then, OC ejects low-temperature (also low-viscosity) fluid into the flow, resulting in a negative μ' . Consequently, $\mu' \partial u' / \partial y$ in the compressible-turbulent interaction term is negative.

E. Near-wall streaks and vortical structures

In this section, the influence of OC on near-wall streaks and coherent structures is further investigated. Figure 10 shows the streamwise velocity fluctuations $\sqrt{\rho} u' / \sqrt{\tau_w}$ at $y_0^* \approx 15$. For each M_b , we consider three cases: uncontrolled, optimal controlled, and the largest y_d^+ . For uncontrolled case [Fig. 10(a)], typical meandering low-speed streak structures are observed aligned along with the streamwise direction. As M_b increases [Figs. 10(b), 10(c)], the streaks become more coherent (longer, wider, and less wavy), and hence more stable. Note that previous works [32,39,48] showed that there is a universal behavior of streaks among different M_b when the semilocal scaling is employed. Compared with the uncontrolled cases, although the streaks still possess typical meandering shapes, their strengths are significantly weakened. For larger y_d^+ case, the near-wall streaks become shorter with clear small-scale undulations, which are the signature of the spanwise vortex rollers shown in Figs. 11(g)–11(i).

The instantaneous vortical structures visualized using λ_ρ criterion [52] for the cases in Fig. 10 are shown in Fig. 11. Numerous slender streamwise vortices are distributed throughout the wall region in uncontrolled cases. And the streamwise vortices are more sparsely distributed and elongated at higher M_b case. Consistent with weakened streaks observed in Fig. 10, the generation of drag-inducing near-wall streamwise vortices is also suppressed for optimally controlled cases, especially for $M_b = 1.5$ case, where much fewer vortices are observed. Surprisingly, in addition to streamwise vortices, organized spanwise rollers are observed in the near-wall region for larger y_d^+ [Figs. 11(g)–11(i)]. Similar structures have been observed for studies of CTCF with an acoustic

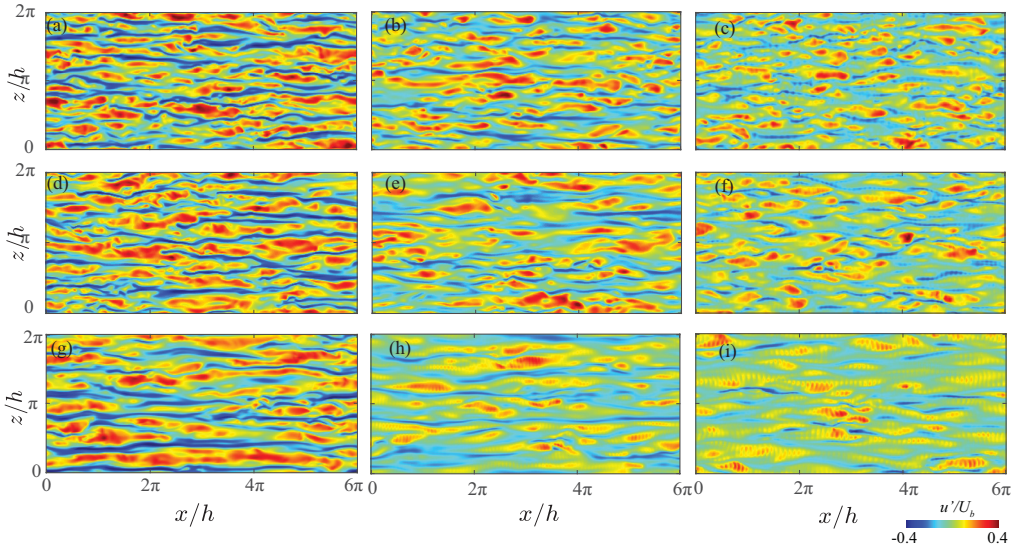


FIG. 10. Instantaneous streamwise velocity fluctuations $\sqrt{\rho}u''/\sqrt{\tau_w}$ at $y_0^* = 15$. Note that the top, middle, and bottom rows denote $M_b = 0.3, 0.8,$ and 1.5 , respectively; and the detecting plane are $y_d^+ = 0, 12.5, 17.5, 0, 17.5, 22.5, 0, 20,$ and 30 for (a)–(i).

impedance boundary condition [53,54]. These structures are mainly trapped in an extremely thin viscous region, which is designated as the resonance buffer layer by Scalo *et al.* [53]. The resonance buffer layer develops due to the Kelvin-Helmholtz instability, which is driven by the interaction of

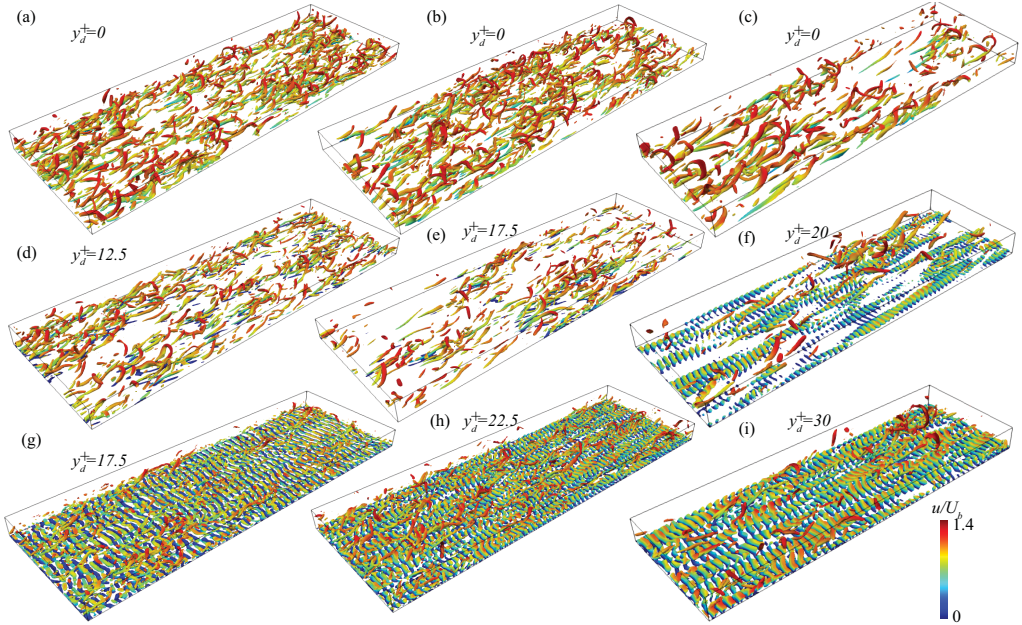


FIG. 11. Vortical structures visualized using λ_ρ criterion for (a)–(c) uncontrolled, (d)–(f) $y_d^+ = 17.5$, and (g)–(i) $y_d^+ = 25$. The left, middle, and right columns correspond to $M_b = 0.3, 0.8$ and 1.5 , respectively.

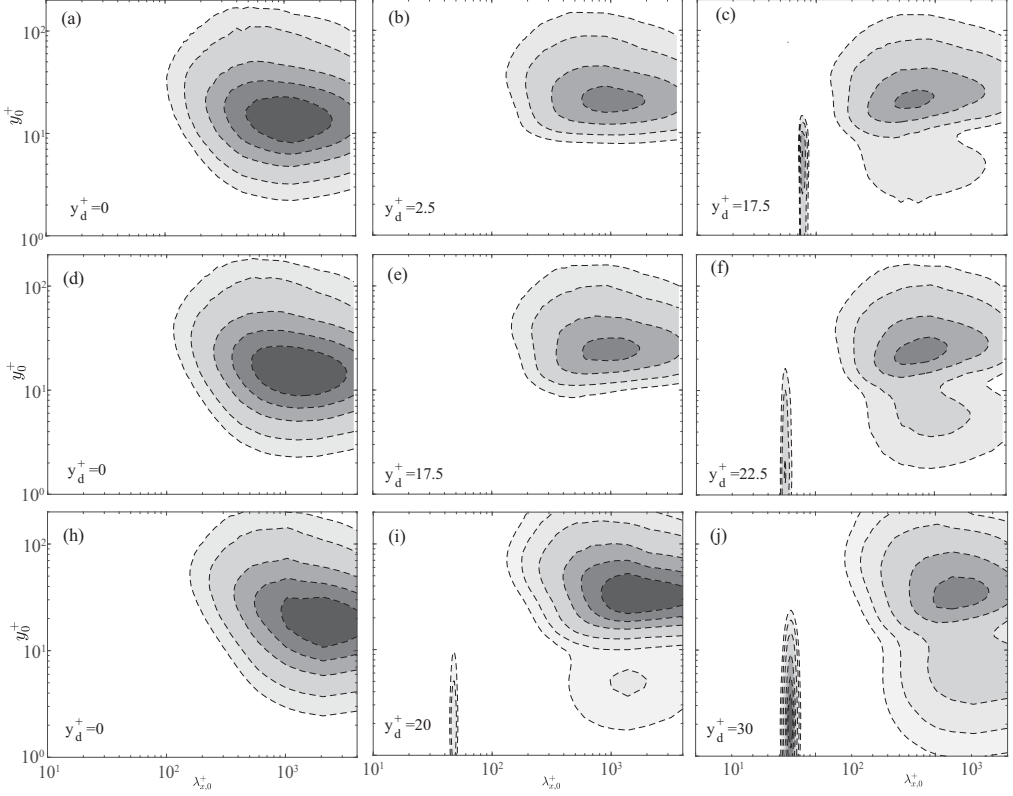


FIG. 12. Premultiplied streamwise spectra of streamwise velocity $k_x E_{\rho u' u'}$ as a function of streamwise wavelength $\lambda_{x,0}^+$ and y_0^+ . The top, middle, and bottom rows correspond to $M_b = 0.3, 0.8,$ and $1.5,$ respectively; and at each $M_b,$ the contour levels are $[0.1 \ 0.2 \ 0.4 \ 0.6 \ 0.8]$ of the maximum value of the uncontrolled case.

the mean shear and the wall-normal wave propagation resulting from resonant excitation of wall blowing and suction. The signature of the spanwise rollers in the resonance buffer layer attributes to the distinct excess of Reynolds shear stresses in the near-wall region [Fig. 7], the main cause for the deterioration of drag reduction.

F. Energy spectra

Figure 12 compares the premultiplied streamwise spectra of streamwise velocity $k_x E_{\rho u' u'}$ (normalized by the maximum value of the uncontrolled case) as a function of streamwise wavelength $\lambda_{x,0}^+$ and y_0^+ between the uncontrolled and controlled cases. For the uncontrolled case, the spectra clearly show the presence of an energetic inner site corresponding to the near-wall streak generation cycle [55]. The peak location of the spectra typically represents the mean length of the streaks. For incompressible flows, the length of near-wall streak is of the order of 10^3 in wall units. Consistent with that shown in Fig. 10, Figs. 12(a), 12(d) 12(h) suggest that the streak length, when scaled in wall units, increases with M_b . In particular, the wavelength of the peak becomes $\lambda_x^+ \approx 1000, 1500,$ and 2000 for $M_b = 0.3, 0.8,$ and 1.5 . Furthermore, the wall-normal location of the peak also slightly increases with M_b , which is consistent with an outward shift of the streamwise Reynolds stress in Fig. 6. For the optimal controlled cases, the energy contribution from the near-wall region is effectively suppressed. In addition, the energy-containing part is shifted towards a smaller wavelength λ_x^+ and larger y_0^+ with a much weaker peak. This is consistent with Fig. 10 showing

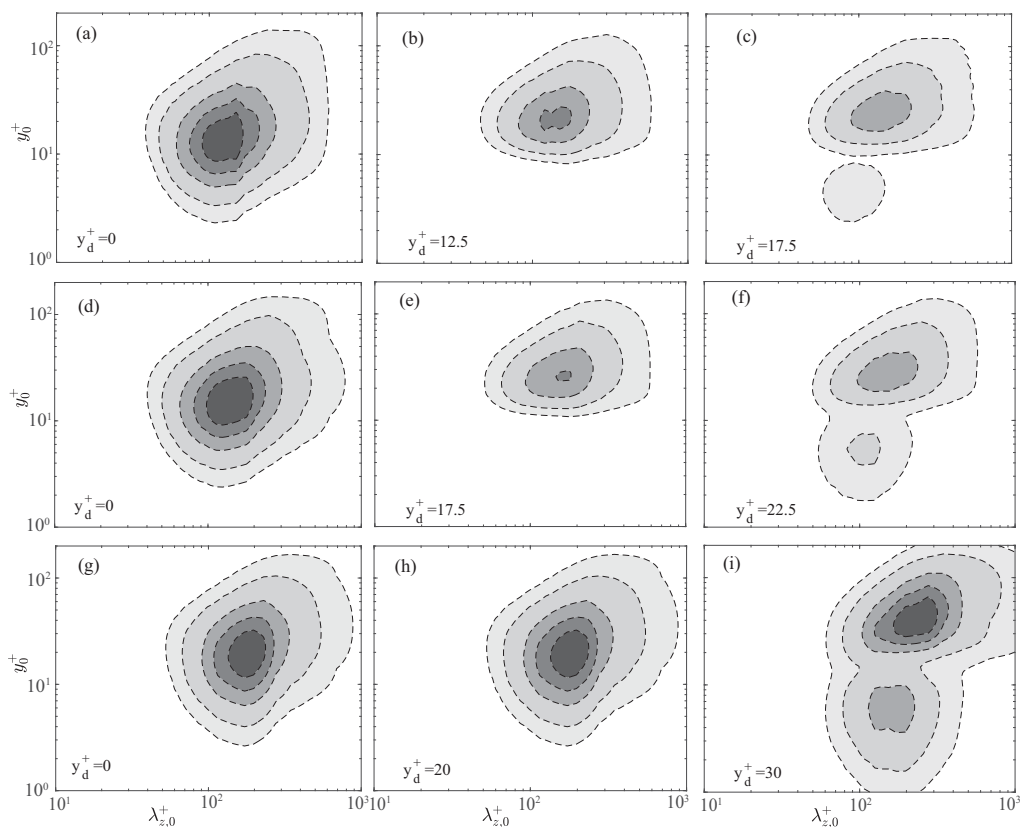


FIG. 13. Premultiplied spanwise spectra of streamwise velocity $k_z E_{\rho u'' u''}$ as a function of spanwise wavelength $\lambda_{x,0}^+$ and y_0^+ . The top, middle, and bottom rows correspond to $M_b = 0.3, 0.8,$ and $1.5,$ respectively; and at each $M_b,$ the contour levels are $(0.1, 0.2, 0.4, 0.6, 0.8)$ of the maximum value of the uncontrolled case.

that the streaks under OC are significantly weakened. However, at large y_d^+ , due to intense blowing and suction, the energy in the near-wall region significantly increases, and a second peak develops close to the wall ($y_0^+ < 10$). In addition, consistent with the near-wall spanwise rollers observed in Figs. 11(c) and 11(e), a spike is observed at the small wavelength λ_x^+ in energy spectra, and the wavelength of the spike remains roughly constant in the wall-normal direction. The wavelength slightly decreases with M_b . The energy content associated with the near-wall spanwise rollers becomes smaller at higher M_b , which is consistent with a smaller inner peak in τ_{11} [Figs. 6(a) and 6(b)]. The characteristics of the resonance layer will be discussed in Sec. VB.

Figure 13 compares the premultiplied spanwise spectra of streamwise velocity $k_z E_{\rho u'' u''}$ (normalized by the maximum value of the uncontrolled case) as a function of the spanwise wavelength $\lambda_{x,0}^+$ and y_0^+ between the uncontrolled and controlled cases; the peak location of the spectrum typically represents the mean streak spacing. For incompressible flows, the near-wall streak spacing in the viscous sublayer is about 10^2 in wall units. Figures 13(a) and 13(d) show that the streak spacing for uncontrolled cases, when scaled in wall units, increases with M_b . Again, for the optimally controlled case, the energy near the wall is significantly suppressed, with the peak shift to large $\lambda_{x,0}^+$ and y_0^+ , suggesting that the streak spacing becomes wider. For large y_d^+ cases, a second peak occurs near the wall, which is much stronger for $M_b = 1.5$ case. Note that the absence of a spanwise periodic

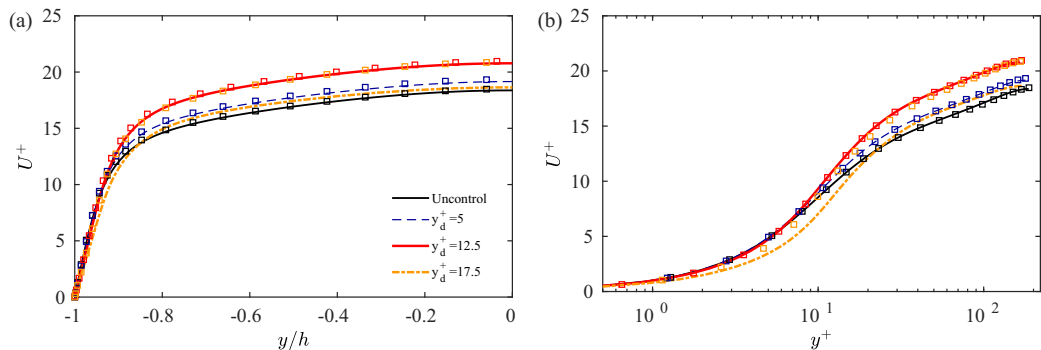


FIG. 14. Mean streamwise velocity U^+ profiles for different y_d^+ cases as a function of (a) y/h and (b) y^+ . Note that the lines and square denotes the strictly incompressible and $M_b = 0.3$ cases, respectively.

signature in the energy spectra indicates that the structures observed in the resonance buffer layer are predominantly two dimensional.

V. DISCUSSION

A. Comparison between the incompressible and the low Mach number cases

Here, we provide a detailed comparison between the low Mach number (i.e., $M_b = 0.3$) and the strictly incompressible cases. Figures 14(a) and 14(b) shows the mean streamwise velocity profiles (U^+) in outer and inner wall unit, respectively. It is clear that U^+ agrees very well between these two cases at low y_d^+ . For $y^+ = 17.5$ case, U^+ for $M_b = 0.3$ is below the strictly incompressible one in the whole range of y . Figures 15(a)–15(d) further show the Reynolds normal (τ_{11} , τ_{22} , and τ_{33}) and shear (τ_{12}) stresses as a function of y_0^+ for different y_d^+ cases, respectively. Again, all the Reynolds stresses collapse between $M_b = 0.3$ and the strictly incompressible cases for low y_d^+ . For $y^+ = 17.5$ case, expect for τ_{33} , all the Reynolds stresses for $M_b = 0.3$ significantly deviates from the incompressible case. In particular, τ_{12} is much larger than the incompressible cases in the near-wall region. Figure 16 shows the instantaneous vortical structures visualized using λ_ρ criterion, which is equivalent to λ_2 here [56], for the incompressible case with different y_d^+ cases. Similar to that observed for $M_b = 0.3$ case [Fig. 11(a)], numerous slender streamwise vortices are distributed throughout the wall region for the uncontrolled case. In addition, the generation of drag-inducing near-wall streamwise vortices become less for $y_d^+ = 10$ case. Interestingly, although the number of streamwise vortices increases at larger y_d^+ , the organized spanwise rollers observed for the compressible cases are not presented, suggesting that the density and viscosity variation in the near wall region is essential for the formation of these rollers. It also confirms that the development of spanwise rollers is the main cause of the increase of Reynolds shear stress and hence drag for the $M_b = 0.3$ case at large y_d^+ .

B. Resonance buffer layer

Flow visualization for large y_d^+ cases in Fig. 11 reveals a remarkable, streamwise-periodic array of spanwise-coherent rollers. In addition, the energy spectra show that these structures are confined in a layer near the wall, with the spacing unchanged along the y direction. Careful inspection shows that these structures are not stationary, and they propagate in the streamwise direction. Hence, the coherent component associated with these structures can be assumed as

$$\hat{\phi}(x, y, \varphi) = \mathcal{F}\left(2\pi\left[\frac{x}{\lambda_x} - f_r t\right]\right) = \mathcal{F}\left(\frac{2\pi}{\lambda_x}[x - c_x t]\right), \quad (11)$$

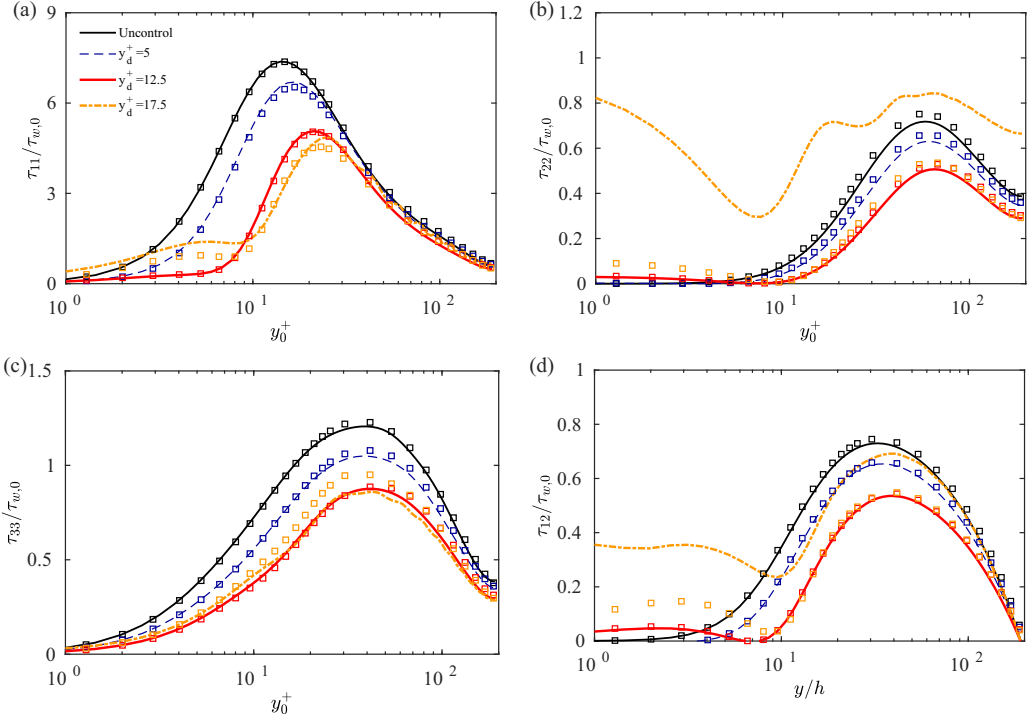


FIG. 15. Reynolds normal and shear stresses components (normalized by the wall-shear stress of the uncontrolled case $\tau_{w,0}$) as a function of y_0^+ for different y_d^+ cases: (a) τ_{11} ; (b) τ_{22} ; (c) τ_{33} , and (d) τ_{12} . Note that the lines and square denote the strictly incompressible and $M_b = 0.3$ cases, respectively.

where \mathcal{F} is a generic periodic function with a fundamental period 2π , $\lambda_x = 2\pi/k_x$ is the streamwise wavelength, $f_r = \omega_r/2\pi$ is the resonance frequency, and c_x is the wave propagation speed. The characteristics of the coherent component can be determined using two-point space-time autocorrelations of wall-normal velocity fluctuations, which is defined as

$$R_{vv}(\Delta x, \Delta \tau, y) = \frac{\overline{v'(x, y, z, t)v'(x + \Delta x, y, z, t + \Delta \tau)}}{v'^2(y)}. \quad (12)$$

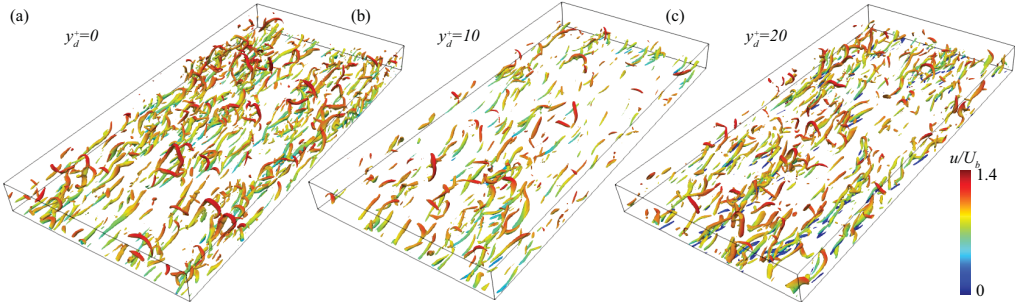


FIG. 16. Vortical structures visualized using λ_ρ criterion for the strictly incompressible case: (a) $y_d^+ = 0$ (uncontrolled), (b) $y_d^+ = 10$, and (c) $y_d^+ = 20$.

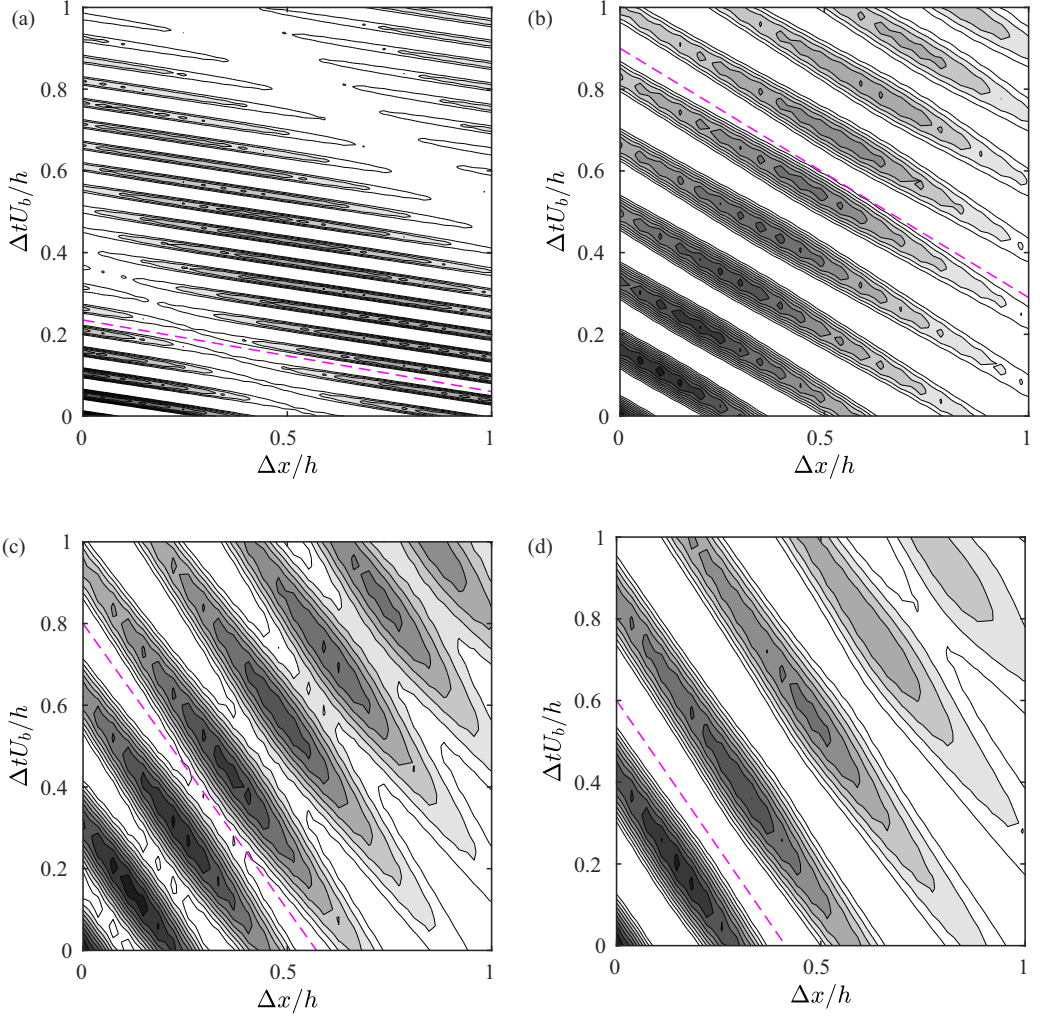


FIG. 17. Space-time correlations of wall-normal velocity $R_{vv}(\Delta x, \Delta \tau, y)$ at $y/h = -0.98$ for (a) $M_b = 0.3$ with $y_d^+ = 17.5$, (b) $M_b = 0.8$ with $y_d^+ = 22.5$, (c) $M_b = 1.5$ with $y_d^+ = 22.5$, and (d) $M_b = 1.5$ with $y_d^+ = 30$.

Figure 17 shows R_{vv} at $y/h = -0.98$ for different M_b cases. The streamwise wavelength λ_x , determined from the peak of $R_{vv}(\Delta x, 0, y)$, decreases with M_b , namely, from 0.34 to 0.24 as M_b increases from 0.3 and 1.5. Note that λ_x here is smaller than that in Ref. [53] (i.e., $\lambda_x = 0.4$). A sensitivity analysis of the computational domain size and grid resolution (Appendix) confirms that the observed value is not a numerical artifact. In addition, the resonance frequency $f_r = 1/\Delta \tau$ also decreases with M_b , from $f_r \approx 16.2$ for $M_b = 0.3$ to $f_r = 2.94$ for $M_b = 1.5$. Note that the resonance frequency observed here are larger than those in Ref. [53], which was prechosen as the frequency of the flow (i.e., $f_r = M_b$). Consequently, the propagation speed $c_x = \lambda_x f_r$ also decreases with M_b . In particular, $c_x = 5.56, 1.65,$ and 0.69 for cases shown in Figs. 17(a)–17(c), respectively, which are comparable to the speed of sound ($c = \sqrt{\gamma RT} = \sqrt{T}/M_b$) in the resonance buffer layer. It is also worth mentioning that, as the temperature, as well as the speed of sound, increases with increasing y_d^+ , the propagation speed c_x is slightly larger at larger y_d^+ (e.g., increases from 0.69 to 0.71 when y_d^+ varies from $y_d^+ = 22.5$ –30 at $M_b = 1.5$). The generation of spanwise rollers at high y_d^+ is very interesting, and a detailed study should be conducted to investigate their genesis and the potential

TABLE IV. Parameters used in the study of domain size effect for the supersonic case at $Re_b = 3000$ and $M_b = 1.5$. Here, C_f values are for the uncontrolled case and DR values are the amount of drag reduction for spanwise wall oscillation with $T^+ = 100$ and $A^+ = 12$.

| Case | $L_x \times L_y \times L_z$ | $N_x \times N_y \times N_z$ | Δx^+ | Δz^+ | DR (%) |
|---------|-----------------------------------|------------------------------|--------------|--------------|--------|
| R3KM15S | $3\pi h \times 2h \times 2\pi h$ | $512 \times 129 \times 256$ | 4.42 | 5.9 | 0.5 |
| R3KM15L | $12\pi h \times 2h \times 2\pi h$ | $1024 \times 129 \times 512$ | 8.84 | 2.95 | 0.2 |

approaches to attenuating them for better drag reduction performance, beyond the scope of the current paper.

VI. CONCLUSION

Inspired by the significant drag reduction achieved in incompressible flows [1], we performed a detailed study of OC in CTCF through DNS. The drag control performance is evaluated at a fixed bulk Reynolds number Re_b of 3000 for three different bulk Mach numbers: $M_b = 0.3, 0.8,$ and 1.5 . For all M_b , DR has a similar trend to that of the incompressible case, namely DR nonmonotonically varies with y_d^+ . Compared with the incompressible case, DR slightly decreases at small y_d^+ but increases at large y_d^+ . Consequently, with increasing M_b , the optimal sensing plane shifts to larger values, and the maximum drag reduction also slightly decreases. In particular, different from the incompressible cases where $y_{d,\text{opt}}^+$ is around 15, $y_{d,\text{opt}}^+$ is 12.5, 17.5, and 20 for $M_b = 0.3, 0.8,$ and 1.5 , respectively; and the DR_{max} is around 23% for all cases. In addition, when scaling the sensing plane with semilocal units, a better collapse on DR is observed between different M_b , especially for low y_d^* . The optimal sensing plane is located at $y_d^* \approx 15$. Study of OC at higher Reynolds numbers [57] showed that the drag performance decreases with increasing Re in incompressible flows, mainly due to the increased contributions of large-scale and very-large-scale structures. It would be interesting to investigate the Reynolds number effect of OC in compressible flows.

Interestingly, for large y_d^+ cases, a resonance buffer layer, characterized by streamwise-periodic array of spanwise-coherent rollers, develops. It is generated due to intense hydroacoustic instabilities resulting from the interaction of high-amplitude wall-normal wave propagation with the background mean shear. Space-time correlation reveals that the resonance buffer layer has a well-defined streamwise wavelength λ_x and resonance frequency f_r ; both of them are found to decrease with M_b . In addition, the coherent structures in the resonance layer travel in the streamwise direction with an advection velocity close to the speed of sound. These near-wall spanwise rollers lead to a significant increase in the Reynolds shear stress near the wall, one of the main reasons for the deterioration in DR for high y_d^+ cases, particularly at low M_b . The temporal and spatial coherence of the resonance buffer layer structures suggests that the triple decomposition via spanwise averaging or phase locking of instantaneous quantities [58] can be fruitful to separate the effect of the wave and random turbulence, as well as their mutual interaction, to be pursued in future. Note that due to the presence of strong coherent wall-normal transpiration, OC for large y_d^+ cases become similar to the drag control using streamwise traveling wave blowing and suction [59,60]. It would be interesting to investigate the similarity of these two control methods.

ACKNOWLEDGMENTS

Computational resources provided by Texas Tech University HPCC, TACC Lonestar, and XSEDE Stampede2 are acknowledged.

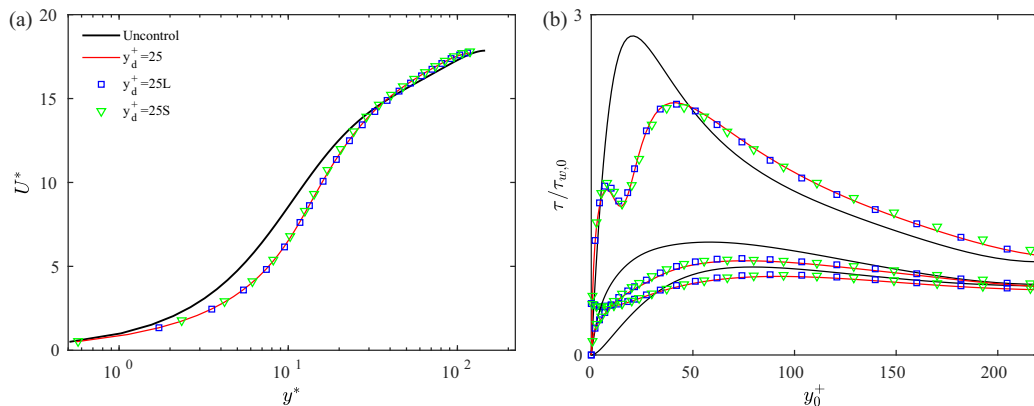


FIG. 18. Comparison of (a) mean streamwise velocity profiles based on Trettel-Larsson transformation, and (b) Reynolds normal stresses components for different domain size cases of $Re_b = 3000$, $M_b = 1.5$ and $y_d^+ = 25$.

APPENDIX: SENSITIVITY TO BOX SIZE AND GRID RESOLUTION

Although the domain size we employed is relatively large, it is still necessary to verify that the observed flow response, particularly the presence of the resonance layer, might be an artifact of the specific computational domain size and grid resolution adopted. Hence, two additional simulations of different computational domain size and grid resolutions are conducted for the supersonic $Re_b = 3000$ and $M_b = 1.5$ case (see Table IV for the details of the simulation parameters). When choosing $y_d^+ = 25$, all cases yield a similar amount of drag reduction. Figure 18 compares the mean velocity profiles based on the Trettel-Larsson transformation and Reynolds normal stresses, where good agreements are observed among different computational domain size cases. Figure 19 shows the streamwise and spanwise autocorrelation of the wall-normal velocity component R_{vv} at $y/h = -0.98$. First, both streamwise and spanwise correlations diminish at large Δx and Δz , suggesting the adequacy of domain size. Furthermore, $R_{vv}(\Delta x)$ exhibits the signature of the spanwise rollers in the resonance buffer layer, and a negligible difference is observed in the streamwise wavelength among different domain size cases, suggesting that the characteristics of the resonance buffer layer determined in the main text do not depend on the particular numerical setup.

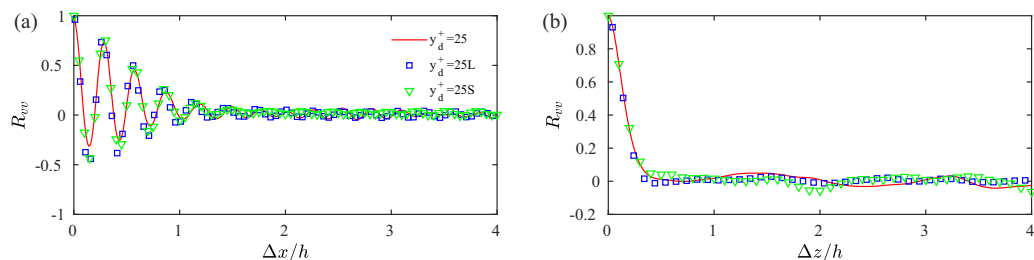


FIG. 19. (a) Streamwise and (b) spanwise two-point autocorrelations correlations of wall-normal velocity R_{vv} at $y/h = -0.98$ for different domain size cases of $Re_b = 3000$, $M_b = 1.5$, and $y_d^+ = 25$.

- [1] H. Choi, P. Moin, and J. Kim, Active turbulence control for drag reduction in wall-bounded flows, *J. Fluid Mech.* **262**, 75 (1994).
- [2] E. Hammond, T. Bewley, and P. Moin, Observed mechanisms for turbulence attenuation and enhancement in opposition-controlled wall-bounded flows, *Phys. Fluids* **10**, 2421 (1998).
- [3] Y. M. Chung and T. Talha, Effectiveness of active flow control for turbulent skin-friction drag reduction, *Phys. Fluids (1994–present)* **23**, 025102 (2011).
- [4] Q.-J. Xia, W.-X. Huang, C.-X. Xu, and G.-X. Cui, Direct numerical simulation of spatially developing turbulent boundary layers with opposition control, *Fluid Dyn. Res.* **47**, 025503 (2015).
- [5] A. Stroh, B. Frohnappfel, P. Schlatter, and Y. Hasegawa, A comparison of opposition control in turbulent boundary layer and turbulent channel flow, *Phys. Fluids* **27**, 075101 (2015).
- [6] D. Gatti and M. Quadrio, Performance losses of drag-reducing spanwise forcing at moderate values of the reynolds number, *Phys. Fluids (1994–present)* **25**, 125109 (2013).
- [7] J. Yao, X. Chen, and F. Hussain, Drag control in wall-bounded turbulent flows via spanwise opposed wall-jet forcing, *J. Fluid Mech.* **852**, 678 (2018).
- [8] Y. Chang, S. S. Collis, and S. Ramakrishnan, Viscous effects in control of near-wall turbulence, *Phys. Fluids* **14**, 4069 (2002).
- [9] K. Iwamoto, Y. Suzuki, and N. Kasagi, Reynolds number effect on wall turbulence: Toward effective feedback control, *Int. J. Heat Fluid Flow* **23**, 678 (2002).
- [10] Y.-S. Wang, W.-X. Huang, and C.-X. Xu, Active control for drag reduction in turbulent channel flow: The opposition control schemes revisited, *Fluid Dyn. Res.* **48**, 055501 (2016).
- [11] C. Lee, J. Kim, and H. Choi, Suboptimal control of turbulent channel flow for drag reduction, *J. Fluid Mech.* **358**, 245 (1998).
- [12] P. Koumoutsakos, Vorticity flux control for a turbulent channel flow, *Phys. Fluids* **11**, 248 (1999).
- [13] M. Pamiès, E. Garnier, A. Merlen, and P. Sagaut, Response of a spatially developing turbulent boundary layer to active control strategies in the framework of opposition control, *Phys. Fluids* **19**, 108102 (2007).
- [14] J. Yao, X. Chen, and F. Hussain, Composite active drag control in turbulent channel flows, *Phys. Rev. Fluids* **6**, 054605 (2021).
- [15] J. Yao, X. Chen, and F. Hussain, Reynolds number effect on drag control via spanwise wall oscillation in turbulent channel flows, *Phys. Fluids* **31**, 085108 (2019).
- [16] C. Lee, J. Kim, D. Babcock, and R. Goodman, Application of neural networks to turbulence control for drag reduction, *Phys. Fluids* **9**, 1740 (1997).
- [17] B.-Z. Han and W.-X. Huang, Active control for drag reduction of turbulent channel flow based on convolutional neural networks, *Phys. Fluids* **32**, 095108 (2020).
- [18] J. Park and H. Choi, Machine-learning-based feedback control for drag reduction in a turbulent channel flow, *J. Fluid Mech.* **904**, A24 (2020).
- [19] J. Lim and J. Kim, A singular value analysis of boundary layer control, *Phys. Fluids* **16**, 1980 (2004).
- [20] M. Luhar, A. S. Sharma, and B. J. McKeon, Opposition control within the resolvent analysis framework, *J. Fluid Mech.* **749**, 597 (2014).
- [21] S. S. Toedtli, M. Luhar, and B. J. McKeon, Predicting the response of turbulent channel flow to varying-phase opposition control: Resolvent analysis as a tool for flow control design, *Phys. Rev. Fluids* **4**, 073905 (2019).
- [22] L. Duan and M. M. Choudhari, Effects of riblets on skin friction and heat transfer in high-speed turbulent boundary layers, in *Proceedings of the 50th AIAA Aerospace Sciences Meeting including the New Horizons Forum and Aerospace Exposition, 9-12 January 2012, Nashville, Tennessee* (AIAA, Reston, VA, 2012), Paper AIAA 2012-1108.
- [23] L. Duan and M. M. Choudhari, Direct numerical simulations of high-speed turbulent boundary layers over riblets, in *Proceedings of the 52nd Aerospace Sciences Meeting, 13-17 January 2014, National Harbor, Maryland* (AIAA, Reston, VA, 2014), Paper AIAA 2014-0934.
- [24] C. Zhe, Y. ChangPing, L. Li, and L. XinLiang, Effect of uniform blowing or suction on hypersonic spatially developing turbulent boundary layers, *Sci. China: Phys., Mech. Astron.* **59**, 664702 (2016).
- [25] Y. Kametani and K. Fukagata, Direct numerical simulation of spatially developing turbulent boundary layers with uniform blowing or suction, *J. Fluid Mech.* **681**, 154 (2011).

- [26] Y. Kametani, K. Fukagata, R. Örlü, and P. Schlatter, Effect of uniform blowing/suction in a turbulent boundary layer at moderate reynolds number, *Int. J. Heat Fluid Flow* **55**, 132 (2015).
- [27] Y. Kametani, A. Kotake, K. Fukagata, and N. Tokugawa, Drag reduction capability of uniform blowing in supersonic wall-bounded turbulent flows, *Phys. Rev. Fluids* **2**, 123904 (2017).
- [28] J. Fang, L.-P. Lu, and L. Shao, Heat transport mechanisms of low mach number turbulent channel flow with spanwise wall oscillation, *Acta Mech. Sin.* **26**, 391 (2010).
- [29] J. Yao and F. Hussain, Supersonic turbulent boundary layer drag control using spanwise wall oscillation, *J. Fluid Mech.* **880**, 388 (2019).
- [30] Y. Morinishi, S. Tamano, and K. Nakabayashi, Direct numerical simulation of compressible turbulent channel flow between adiabatic and isothermal walls, *J. Fluid Mech.* **502**, 273 (2004).
- [31] G. N. Coleman, J. Kim, and R. Moser, A numerical study of turbulent supersonic isothermal-wall channel flow, *J. Fluid Mech.* **305**, 159 (1995).
- [32] J. Yao and F. Hussain, Turbulence statistics and coherent structures in compressible channel flow, *Phys. Rev. Fluids* **5**, 084603 (2020).
- [33] A. Trettel and J. Larsson, Mean velocity scaling for compressible wall turbulence with heat transfer, *Phys. Fluids* **28**, 026102 (2016).
- [34] D. Modesti and S. Pirozzoli, Reynolds and mach number effects in compressible turbulent channel flow, *Int. J. Heat Fluid Flow* **59**, 33 (2016).
- [35] P. Huang, G. Coleman, and P. Bradshaw, Compressible turbulent channel flows: Dns results and modelling, *J. Fluid Mech.* **305**, 185 (1995).
- [36] X. Chen, J. Yao, and F. Hussain, Theoretical framework for energy flux analysis of channels under drag control, *Phys. Rev. Fluids* **6**, 013902 (2021).
- [37] M. Lee and R. D. Moser, Direct numerical simulation of turbulent channel flow up to re 5200, *J. Fluid Mech.* **774**, 395 (2015).
- [38] J. Kim, P. Moin, and R. Moser, Turbulence statistics in fully developed channel flow at low reynolds number, *J. Fluid Mech.* **177**, 133 (1987).
- [39] A. Patel, B. J. Boersma, and R. Pecnik, The influence of near-wall density and viscosity gradients on turbulence in channel flows, *J. Fluid Mech.* **809**, 793 (2016).
- [40] H. Foysi, S. Sarkar, and R. Friedrich, Compressibility effects and turbulence scalings in supersonic channel flow, *J. Fluid Mech.* **509**, 207 (2004).
- [41] E. V. Driest, Turbulent boundary layer in compressible fluids, *J. Aeronaut. Sci.* **18**, 145 (1951).
- [42] L. Duan, I. Beekman, and M. Martin, Direct numerical simulation of hypersonic turbulent boundary layers. Part 2. effect of wall temperature, *J. Fluid Mech.* **655**, 419 (2010).
- [43] S. Pirozzoli and M. Bernardini, Turbulence in supersonic boundary layers at moderate reynolds number, *J. Fluid Mech.* **688**, 120 (2011).
- [44] A. Hadjadj, O. Ben-Nasr, M. Shadloo, and A. Chaudhuri, Effect of wall temperature in supersonic turbulent boundary layers: A numerical study, *Int. J. Heat Mass Transf.* **81**, 426 (2015).
- [45] B.-Q. Deng, C.-X. Xu, W.-X. Huang, and G.-X. Cui, Strengthened opposition control for skin-friction reduction in wall-bounded turbulent flows, *J. Turbul.* **15**, 122 (2014).
- [46] W. Jung, N. Mangiavacchi, and R. Akhavan, Suppression of turbulence in wall-bounded flows by high-frequency spanwise oscillations, *Phys. Fluids A: Fluid Dyn.* **4**, 1605 (1992).
- [47] D. Gatti and M. Quadrio, Reynolds-number dependence of turbulent skin-friction drag reduction induced by spanwise forcing, *J. Fluid Mech.* **802**, 553 (2016).
- [48] L. Sciacovelli, P. Cinnella, and X. Gloerfelt, Direct numerical simulations of supersonic turbulent channel flows of dense gases, *J. Fluid Mech.* **821**, 153 (2017).
- [49] E. Hurst, Q. Yang, and Y. M. Chung, The effect of reynolds number on turbulent drag reduction by streamwise travelling waves, *J. Fluid Mech.* **759**, 28 (2014).
- [50] K. Fukagata, K. Iwamoto, and N. Kasagi, Contribution of reynolds stress distribution to the skin friction in wall-bounded flows, *Phys. Fluids (1994–present)* **14**, L73 (2002).
- [51] T. Gomez, V. Flutet, and P. Sagaut, Contribution of reynolds stress distribution to the skin friction in compressible turbulent channel flows, *Phys. Rev. E* **79**, 035301(R) (2009).

- [52] J. Yao and F. Hussain, Toward vortex identification based on local pressure-minimum criterion in compressible and variable density flows, *J. Fluid Mech.* **850**, 5 (2018).
- [53] C. Scalo, J. Bodart, and S. K. Lele, Compressible turbulent channel flow with impedance boundary conditions, *Phys. Fluids* **27**, 035107 (2015).
- [54] R. Sebastian, D. Marx, and V. Fortuné, Numerical simulation of a turbulent channel flow with an acoustic liner, *J. Sound Vib.* **456**, 306 (2019).
- [55] W. Schoppa and F. Hussain, Coherent structure generation in near-wall turbulence, *J. Fluid Mech.* **453**, 57 (2002).
- [56] J. Jeong and F. Hussain, On the identification of a vortex, *J. Fluid Mech.* **285**, 69 (1995).
- [57] B.-Q. Deng, W.-X. Huang, and C.-X. Xu, Origin of effectiveness degradation in active drag reduction control of turbulent channel flow at $re\tau = 1000$, *J. Turbul.* **17**, 758 (2016).
- [58] W. Reynolds and A. Hussain, The mechanics of an organized wave in turbulent shear flow. Part 3. theoretical models and comparisons with experiments, *J. Fluid Mech.* **54**, 263 (1972).
- [59] C. Lee, T. Min, and J. Kim, Stability of a channel flow subject to wall blowing and suction in the form of a traveling wave, *Phys. Fluids* **20**, 101513 (2008).
- [60] R. Moarref and M. R. Jovanović, Controlling the onset of turbulence by streamwise travelling waves. Part 1. receptivity analysis, *J. Fluid Mech.* **663**, 70 (2010).